JOURNAL OF COMPUTATIONAL PHYSICS **136,** 399–410 (1997)
ARTICLE NO. CP975755

Cell Aspect Ratio Dependence of Anisotropy Measures for Resolved and Subgrid Scale Stresses

Hans-Jakob Kaltenbach

Department 3, Mathematics, MA 6-3, Technical University Berlin, 10623 Berlin, Germany
E-mail: Kalten@math.tu-berlin.de

Received November 4, 1996; revised May 6, 1997

Discrete approximation of a flow field using anisotropic meshes causes ''unphysical'' anisotropy of the resolved part of the Reynolds stress tensor and of the subgrid scale stress tensor if common anisotropy measures such as $\overline{u_i u_j}/q^2 - 1/3\delta_{ij}$ are used in order to characterize the turbulence structure. By evaluating model spectrum tensors the effect is investigated for isotropic and anisotropic turbulence. The deviation from a physical meaningful anisotropy state depends on various parameters such as the energy spectrum shape near the cutoff in wavespace, the cell aspect ratios, and the range of scales which are resolved. Subgrid kinetic energy must be distributed unequally among the normal stresses on an anisotropic mesh. For example, for aspect ratios $\Delta x : \Delta y : \Delta z = 1 : 8 : 4$, rms fluctuations of subgrid motions are shown to deviate by 9% in isotropic turbulence in the inertial subrange.

1. INTRODUCTION

Flows with strong inhomogeneities of mean quantities are usually approximated on anisotropic meshes. Cell aspect ratios such as the ratio of streamwise and wall-normal spacing, $a_{xy} = \Delta x/\Delta y$, reach values up to 10 close to walls and in other zones with strong shear. This is a direct consequence of the need to have comparable truncation errors in each coordinate direction. Anisotropic grids are suitable for laminar flow simulation as well as for simulations based on the Reynolds averaged Navier–Stokes (RANS) equations where the dependent variables vary smoothly on the grid scale. Similarly, anisotropic grids are often used in direct (DNS) as well as in large eddy simulations (LES) of inhomogeneous turbulent flows—although with generally smaller aspect ratios than in simulations that solve for mean flow variables only.

Early LES on coarse grids used equidistant meshes with moderate aspect ratios. The aspect ratio a_{xy} was 2.5 in the channel flow LES of [2] and 3.7 in the LES of [10]. Part of the success of these simulations comes from the fact that the near wall zone is modeled. The maximum gradient dU/dy of the mean velocity does not have to be resolved numerically but enters as a boundary condition in the form of a wall stress. Turbulent motion in the cells adjacent to the walls is treated in a statistical manner. In this approach—which is at present the only one feasible for Reynolds numbers based on a shear-layer thickness on the order of 10^5—the mesh spacing is necessarily coarse (several hundreds of wall units) and subgrid scales (SGS) contribute up to 40% to the turbulent kinetic energy; see [10]. With increasing computer power a ''wall-resolving'' LES became feasible [6]. This approach is particularly attractive if it is combined with the dynamic subgrid-scale model [3] because it offers a closure which is virtually free from any model parameters. Since the steep mean flow gradients must be resolved in a wall-resolving LES the vertical spacing is restricted to a few wall units in the near wall region. Grid point savings over DNS are achieved mainly by increasing streamwise and spanwise spacing up to $\Delta x^+ = 200$ and $\Delta z^+ = 40$ [7]. Hence, on these grids rather high cell aspect ratios $a_{xy} = 25$ and $a_{zy} = 4$ are encountered at locations around $y^+ = 15$. However, the SGS contributions often do not exceed 10% of the total kinetic energy in this approach.

Grid anisotropy in the context of LES has been addressed by [10, 11]. The primary concern of both studies was how grid anisotropy affects the SGS model. Corrections for the evaluation of the strain rate tensor as well as modifications of the model constant in the Smagorinksy closure were proposed. Reference [5] discusses several issues arising from the use of anisotropic filters such as the fact that anisotropic filtering of an isotropic field results in an anisotropic filtered field.

The goal of the present study is to quantify the consequences of defining resolved scale and SGS fields through an anisotropic grid filter. Using purely kinematic considerations we investigate how anisotropy measures for resolved and subgrid Reynolds stresses depend on cell aspect ratios. Our approach is similar to that used by [11]. By integrating model energy spectrum tensors over anisotropic subdomains of the wavespace we obtain resolved and SGS fields for which we evaluate anisotropy measures. The focus of the study is on the Reynolds stress level, although the impact of anisotropic filtering on higher-order statistics such as strains is known to be even more significant. In

0021-9991/97 $25.00

practice, a LES will be regarded as successful if mean flow and turbulent stresses are predicted with sufficient accuracy. Therefore we restrict our analysis to these quantities of primary interest.

The paper is organized in the following way: after defining anisotropy measures in Section 2 we demonstrate the effect of grid anisotropy in Section 3 using the Euler equations, i.e., inviscid random phase motion which can be simulated with a strictly energy-conserving numerical method. Section 4 extends the investigation to isotropic and anisotropic turbulence following a given model spectrum. In Section 5 we derive SGS stresses for an LES in which the anisotropic grid filter cuts through the inertial subrange.

2. ANISOTROPY MEASURES FOR RESOLVED AND SUBGRID SCALES

We adopt the point of view that cutoff in Fourier space is an appropriate way to define the grid filter in LES. Although this definition is exact in the context of a spectral Navier–Stokes solver only, we think that it is adequate for finite-volume or finite-difference codes which treat the advective terms in an energy-conserving manner. In these methods the solution is not affected by inherent filtering from numerical viscosity and all modes up to the Nyquist frequency will be excited. Our numerical example in Section 3 shows indeed that results obtained with a second-order finite-volume method match closely analytical predictions for energy distribution up to the cutoff wavenumber. Since our considerations are purely kinematic they are not affected by well-known shortcomings of low order, centered finite-difference schemes such as phase errors.

The energy spectrum tensor $\Phi_{ij}(\mathbf{x}, \mathbf{k})$ is defined as a three-dimensional Fourier transform of the two-point correlation tensor $P_{ij}(\mathbf{x}, \mathbf{r}) = \langle u_i(\mathbf{x}) u_j(\mathbf{x} + \mathbf{r}) \rangle$, where the brackets denote an ensemble average. In homogeneous turbulence P_{ij} and

$$\Phi_{ij}(\mathbf{k}) = \left(\frac{1}{2\pi}\right)^3 \int P_{ij}(\mathbf{r}) \exp^{-i\,\mathbf{k}\cdot\mathbf{r}}\, d^3\mathbf{r} \tag{1}$$

are independent of location. Using the continuity condition $k_i \Phi_{ij} = 0$ the energy spectrum tensor for three-dimensional, isotropic turbulence as a function of the scalar energy spectrum function $E(k)$ was derived in [1] as

$$\Phi_{ij}(\mathbf{k}) = \frac{E(k)}{4\pi k^2}\left(\delta_{ij} - \frac{k_i k_j}{k^2}\right). \tag{2}$$

The bracketed term in Eq. (2) stems from the projection operator which ensures zero divergence. In two dimensions the prefactor in Eq. (2) is $E(k)/(\pi k)$. We will use the 2D case as a simple example for which analytical expressions can be obtained and for which numerical tests can be performed cheaply. The scalar energy density satisfies

$$\frac{1}{2} q^2 = \frac{1}{2} \overline{u_i u_i} = \int_0^\infty E(k)\, dk; \tag{3}$$

i.e., the area under the curve $E(k)$ represents the kinetic energy $q^2/2$ and $E(k)\, dk$ collects all contributions from Fourier modes in a spherical shell (3D) or a ring (2D) in $\mathbf{k}$-space of radius k and thickness dk.

For a given spectrum tensor Φ_{ij} we define resolved scale stresses R_{ij} by integrating over the rectangular $\mathbf{k}$-space subregion $|k_x| < N_x$, $|k_y| < N_y$, $|k_z| < N_z$ according to

$$R_{ij} = \langle \overline{u}_i \overline{u}_j \rangle = \int_{-N_x}^{N_x} \int_{-N_y}^{N_y} \int_{-N_z}^{N_z} \Phi_{ij}(\mathbf{k})\, dk_x\, dk_y\, dk_z. \tag{4}$$

The corresponding computational domain will be a cube of side length $L = 2\pi$ with $k_i = 2\pi/L n_i$ as integer wavenumbers. The cell aspect ratio a_{xy} is equal to the inverse of the cutoff wavenumber ratio; i.e., $a_{xy} = \Delta x/\Delta y = N_y/N_x$. Subgrid scale stresses τ_{ij} are obtained by integrating Φ_{ij} over the ''exterior'' part of the wavenumber space which extends to infinity. Common anisotropy measures are

$$B_{ij} = \frac{R_{ij}}{E} - \frac{1}{3}\delta_{ij} \quad \text{and} \quad b_{ij} = \frac{\tau_{ij}}{e} - \frac{1}{3}\delta_{ij}, \tag{5}$$

where $E = R_{ii}$ and $e = \tau_{ii}$ denote turbulent kinetic energy of resolved and SGS motion, respectively. We will frequently quantify the anisotropy of normal stresses by computing ratios of rms values of resolved scale or SGS motions, e.g., $(R_{11}/R_{22})^{1/2} = \overline{u}_1'/\overline{u}_2'$ or $(\tau_{11}/\tau_{22})^{1/2}$. A scale-dependent anisotropy measure

$$\beta_{12}(k) = \left(\frac{E_{11}(k)}{E_{22}(k)}\right)^{1/2} \tag{6}$$

is obtained from radial variance spectra E_{ii} (no summation on i) which collect contributions of a single velocity component u_i to a spherical shell centered at the origin of wavespace. Common practice in LES on grids with unequal sides is to define an equivalent grid scale [2] such as

$$\Delta_{\text{eq}} = (\Delta_x \Delta_y \Delta_z)^{1/3}. \tag{7}$$

Now, using the corresponding cutoff wavenumber $k_{\text{eq}} = 2\pi/\Delta_{\text{eq}}$ it is instructive to measure anisotropy of resolved and SGS motion as

$$\frac{\overline{u}_1'}{\overline{u}_2'} = \sqrt{\frac{\int_0^{k_{eq}} E_{uu}(k)\,dk}{\int_0^{k_{eq}} E_{vv}(k)\,dk}} \quad \text{and}$$
$$\sqrt{\frac{\tau_{11}}{\tau_{22}}} = \sqrt{\frac{\int_{k_{eq}}^{\infty} E_{uu}(k)\,dk}{\int_{k_{eq}}^{\infty} E_{vv}(k)\,dk}}. \tag{8}$$

Rms ratios derived from R_{ij} and τ_{ij} defined by Eq. (4) will deviate from the ones defined by Eq. (8) unless the **k**-space subregion is a cube with $N_x = N_y = N_z$. As noted by [5] a mere consequence of dividing an *isotropic* turbulence field in resolved and subgrid scales using an *anisotropic* filter is the fact that resolved stresses as well as SGS stresses will be *anisotropic* if the anisotropy measure is based on Eq. (5). This is somehow counterintuitive since the original undecomposed field was isotropic and one would expect the same for both subfields. This ''artificial'' anisotropy is a possible source for wrongful interpretation of simulation or filtered experimental data. The underlying reason for this behavior is the continuity constraint being imposed on the energy spectrum tensor as explained in more detail in Section 3.

If both resolved and SGS stresses are known the remedy is to compute total stresses $\sigma_{ij} = R_{ij} + \tau_{ij}$, on which anisotropy measures are based. This is, however, often not possible in practice. Many of the SGS models currently in use lack information about SGS kinetic energy or normal stresses. One often relies solely on resolved scale statistics when comparing with measurements. Under certain assumptions it is possible to estimate the SGS kinetic energy from the SGS eddy viscosity of an actual LES [9]. It is then practice to equally split the estimated SGS energy among the three normal stresses τ_{11}, τ_{22}, τ_{33}. This procedure does not give the correct total stresses in the case of anisotropic meshes. In Section 5 we show how the energy must be split correctly in the case of anisotropic cutoff in the inertial subrange.

Fortunately, the effect described above will be small if energy peak and cutoff are sufficiently far apart in wavenumber space. In the remainder of this study we will quantify the consequences of anisotropic grid filtering by evaluating anisotropy measures for model energy spectrum tensors.

3. GRID ANISOTROPY IN THE CASE OF "INVISCID" ENERGY DISTRIBUTION

3.1. *Two-Dimensional Euler Flow: Analytical Results*

As a first example we consider anisotropic representation of random phase Fourier modes in the absence of viscosity. The kinetic energy of such a velocity field will be distributed equally in wavenumber space, corresponding to scalar spectrum functions $E(k) \approx k^2$ in 3D and $E(k) \approx k$ in 2D, respectively. For $E(k) = c\pi k$, where c is a constant with units of energy times length squared, Eq. (4) with Φ_{ij} from Eq. (2) reduces in 2D to

$$R_{11} = c \int_{-N_x}^{N_x} \int_{-N_y}^{N_y} (1. - k_x^2/(k_x^2 + k_y^2))\,dk_x\,dk_y,$$
$$R_{22} = c \int_{-N_x}^{N_x} \int_{-N_y}^{N_y} (1. - k_y^2/(k_x^2 + k_y^2))\,dk_x\,dk_y. \tag{9}$$

Integration with $N_y = a_{xy}N_x$ yields the ratio of ''resolved scale'' velocity fluctuations as a function of grid anisotropy a_{xy} as

$$\sqrt{\frac{R_{11}}{R_{22}}} = \frac{\overline{u}'}{\overline{v}'} = \sqrt{\frac{a_{xy} + a_{xy}^2\,\pi/2 - (1. + a_{xy}^2)\arctan(a_{xy})}{a_{xy} - a_{xy}^2\,\pi/2 + (1. + a_{xy}^2)\arctan(a_{xy})}}. \tag{10}$$

Even for a moderate cell aspect ratio $a_{xy} = 0.5$ the ratio $\overline{u}'/\overline{v}' = 0.675$ deviates more than 30% from the ''correct'' isotropic value of 1.0 which would result on a grid with $a_{xy} = 1.0$. This unphysical anisotropy is a result of the continuity equation being enforced on an anisotropic mesh and affects only the modes whose wavevector is longer than the minimum cutoff N_y. For these ''corner modes'' the shells (or rings) in wavespace are incomplete. Scales with $k = (k_x^2 + k_y^2)^{1/2}$ smaller than N_y are isotropic in terms of $\beta_{12}(k)$ (Eq. (6)) as can be seen from comparing radial component spectra $E_{11}(k)$ and $E_{22}(k)$; see Fig. 1. Conversely, for the part of the variance spectra where the shells are depleted the measure $\beta_{12}(k)$ will deviate significantly from 1.

These radial spectra follow from integration of the spectrum tensor given in polar coordinates over a given shell surface according to

$$E_{ii}(k) = 4 \int_{\theta_a}^{\theta_b} \Phi_{ii}(k, \theta)\,k\,d\theta \quad \text{(no summation on } i\text{)}. \tag{11}$$

Using $k_x = k\cos\theta$, $k_y = k\sin\theta$, where θ denotes the angle between the k_x-axis and the wavevector, the spectrum tensor reads

$$\Phi_{11}(k, \theta) = \frac{E(k)}{\pi k}(1 - \cos^2\theta) = c\sin^2\theta,$$
$$\Phi_{22}(k, \theta) = \frac{E(k)}{\pi k}(1 - \sin^2\theta) = c\cos^2\theta, \tag{12}$$

for the inviscid case. The integration bounds θ_a, θ_b depend on shell radius k and cutoff wavenumbers N_x, N_y according to

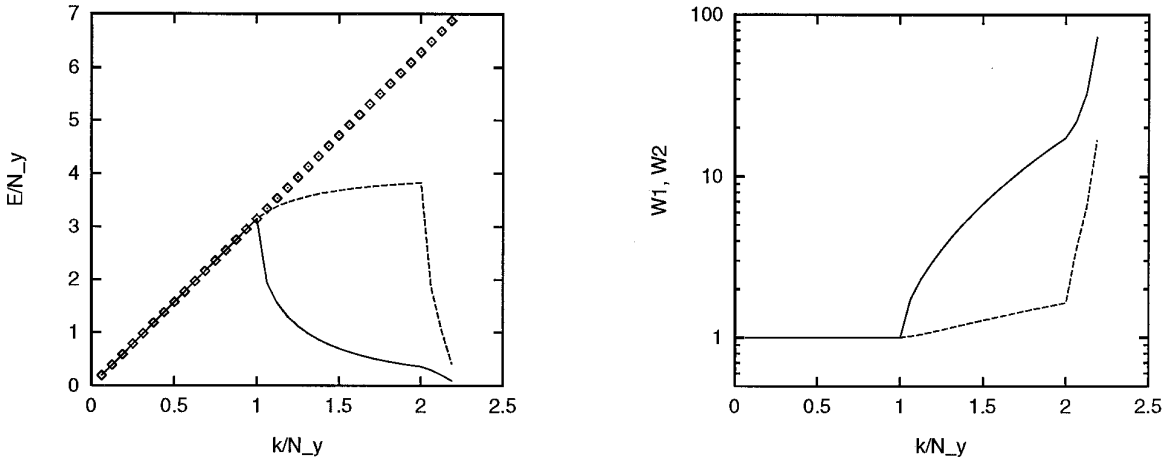

FIG. 1. Left: Radial spectra E_{11}/N_y (—) and E_{22}/N_y (- - -) versus k/N_y for inviscid 2D turbulence approximated with $a_{xy} = 0.5$. Compensated spectra $E_{11} \times W_1$, $E_{22} \times W_2$ are marked with $\diamond$. Right: Weights $W_1(k)$ (—) and $W_2(k)$ (---) are shown.

$$
\begin{aligned}
\text{for } k < N_y: \quad & \theta_a = 0, \quad \theta_b = \frac{\pi}{2}, \\
\text{for } N_y < k < N_x: \quad & \theta_a = 0, \\
& \theta_b = \frac{\pi}{2} - \arccos\left(\frac{N_y}{k}\right), \qquad (13) \\
\text{for } N_x < k < (N_x^2 + N_y^2)^{1/2}: \quad & \theta_a = \arccos\left(\frac{N_x}{k}\right), \\
& \theta_b = \frac{\pi}{2} - \arccos\left(\frac{N_y}{k}\right).
\end{aligned}
$$

In order to see more clearly how an anisotropic grid filter (i.e., a discrete representation on an anisotropic mesh) affects an individual velocity component it is instructive to study the components of Φ_{ij} in the k_x, k_y-plane; see Fig. 2. Equation (12) states that the contribution of a particular segment of shell k to the shell-integrated value of Φ_{ii} (no summation on i) depends on the wavevector orientation and is different for each tensor component. This is a consequence of the projection operator and can also be seen from continuity in wavespace, i.e., $k_x\hat{u}(k_x, k_y) + k_y\hat{v}(k_x, k_y) = 0$, which states that $\hat{u}$ (and consequently $\Phi_{11} = \hat{u}\hat{u}^*$) becomes zero for k_y approaching zero for arbitrary k_x. Vice versa, Φ_{22} is small in the vicinity of the k_y-axis. Because of this uneven distribution inside a given shell Φ_{11} and Φ_{22} are affected differently by an anisotropic filter. Figure 2 depicts the effect of filtering for a shell k lying between the cutoffs N_y and N_x. Whereas the "high-intensity" region of Φ_{11} lies outside the rectangle defined by the cutoff wavenumbers, the segments contributing most to Φ_{22} are not affected by the filter since they are concentrated near the k_x-axis.

As for radial spectra the one-dimensional spectra follow simple analytical expressions

$$
\begin{aligned}
E_{11}(k_x) &= c \int_{-N_y}^{N_y} (1. - k_x^2/(k_x^2 + k_y^2))\, dk_y \\
&= 2c\left(N_y - k_x \arctan\frac{N_y}{k_x}\right), \\
E_{22}(k_x) &= c \int_{-N_y}^{N_y} (1. - k_y^2/(k_x^2 + k_y^2))\, dk_y \\
&= 2ck_x \arctan\frac{N_y}{k_x}, \qquad (14) \\
E_{11}(k_y) &= 2ck_y \arctan\frac{N_x}{k_y}, \\
E_{22}(k_y) &= 2c\left(N_x - k_y \arctan\frac{N_x}{k_y}\right).
\end{aligned}
$$

These are plotted in Fig. 3. Transverse spectra $E_{11}(k_y)$ and $E_{22}(k_x)$—which are identical in a true isotropic representation—deviate from each other even for wavenumbers smaller than the minimum cutoff N_y. This is the well-known aliasing effect; i.e., energy from the high-wavenumber end of direction k_x appears under a different wavenumber in the k_y direction. The example shows that one-dimensional spectra obtained from LES with anisotropic cutoff must be interpreted carefully.

3.2. *Numerical Simulation of 2D Euler Flow*

Before moving on to a 3D case we compare the analytical result (Eq. (10)) with the outcome of a numerical experiment. Simulations were carried out on a square domain

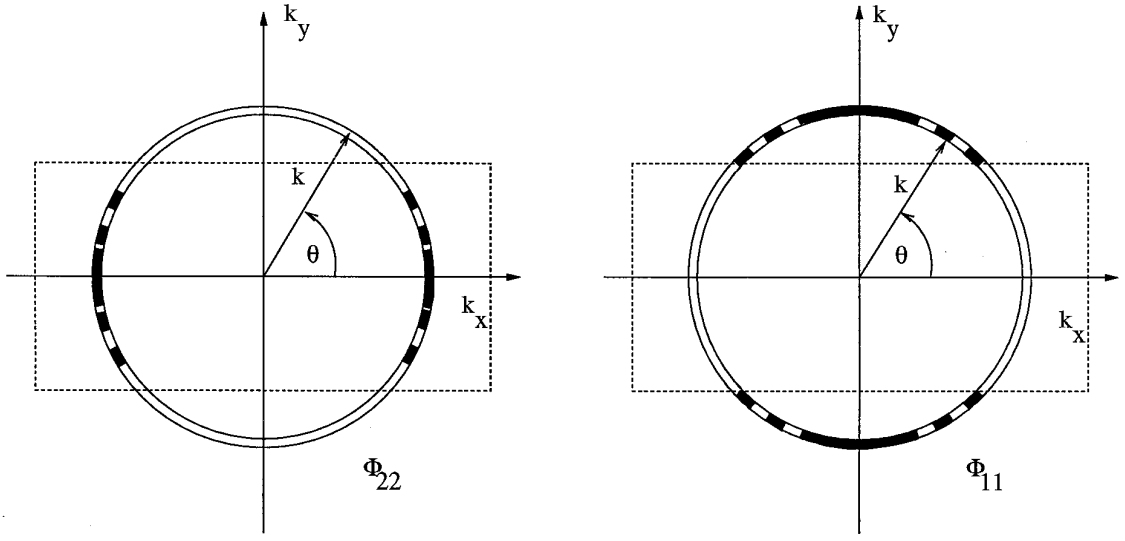

FIG. 2. Sketch of spectrum tensor components Φ_{22} (left) and Φ_{11} (right) of two-dimensional, isotropic turbulence in the k_x, k_y-plane for a shell of radius k. Dark areas mark regions of high intensity. Dotted lines border the region of k-space covered by an anisotropic filter with $N_x = 2N_y$.

with 64×32 meshes using a kinetic-energy-conserving, incompressible Navier–Stokes solver with a second-order discretization on a staggered mesh. No viscous terms and no numerical dissipation were present in these simulations.

Figure 4 depicts the temporal evolution of the rms ratio $\overline{u}'/\overline{v}'$ for two different initial fields. Both initial fields were created using a random potential Ψ: in the first case the potential was initialized in a small wavenumber band below the smaller of both cutoff wavenumbers of the discrete approximation. A velocity field with zero divergence is derived as $u = \partial\Psi/\partial y$ and $v = -\partial\Psi/\partial x$. Since the initial field contains large scales only it is isotropic. As the energy spectrum tensor is gradually reaching equilibrium the ratio $\overline{u}'/\overline{v}'$ becomes independent of the initial condition and fluctuates around 0.64. This is slightly below the value of 0.675 predicted by Eq. (10).

In the second case Ψ was initialized with white noise. The initial rms ratio of such a field is directly related to the grid anisotropy; i.e., $\overline{u}'/\overline{v}'|_{t=0} = a_{xy} = 0.5$. For this case the initial energy distribution is closer to the final equilibrium state and the asymptotic velocity ratio is reached more quickly than in the first case. These numerical experiments show that the effects predicted in Eq. (10) describe phe-

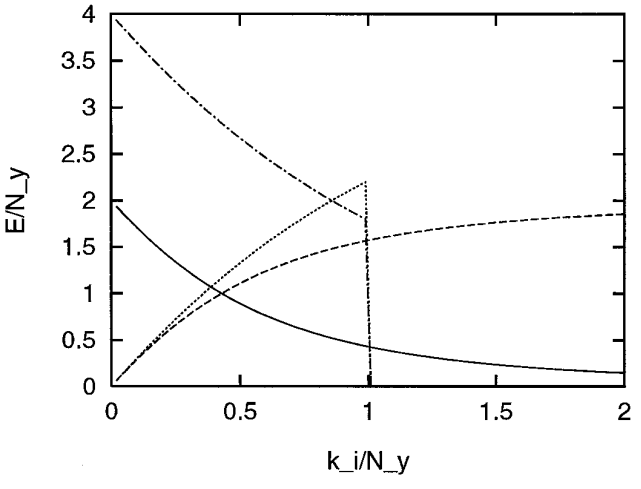

FIG. 3. One-dimensional spectra $E_{11}/N_y(k_x)$ (—), $E_{22}/N_y(k_x)$ (---), $E_{11}/N_y(k_y)$ (· · ·), and $E_{22}/N_y(k_y)$ (—·—·) versus k_i/N_y for inviscid 2D random phase turbulence approximated with $a_{xy} = 0.5$.

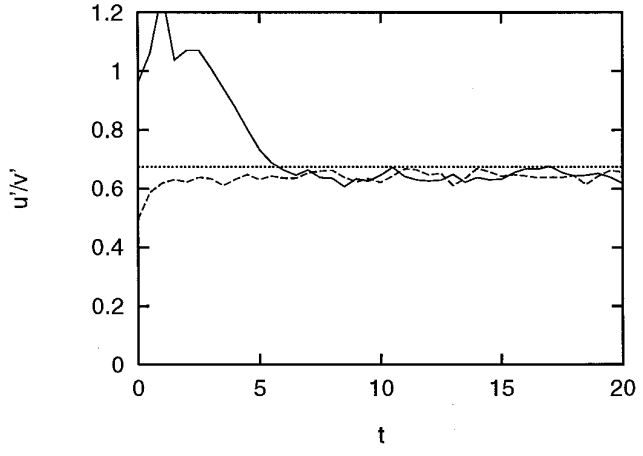

FIG. 4. Rms velocity ratio $\overline{u}'/\overline{v}'$ from inviscid 2D simulation with $a_{xy} = 0.5$ for initial values $\overline{u}'/\overline{v}' = 1$. (—) and $\overline{u}'/\overline{v}' = 0.5$ (---) versus time normalized by $L_{\text{box}}/(\sqrt{2}\pi q)$. Prediction from Eq. (10) (· · ·).

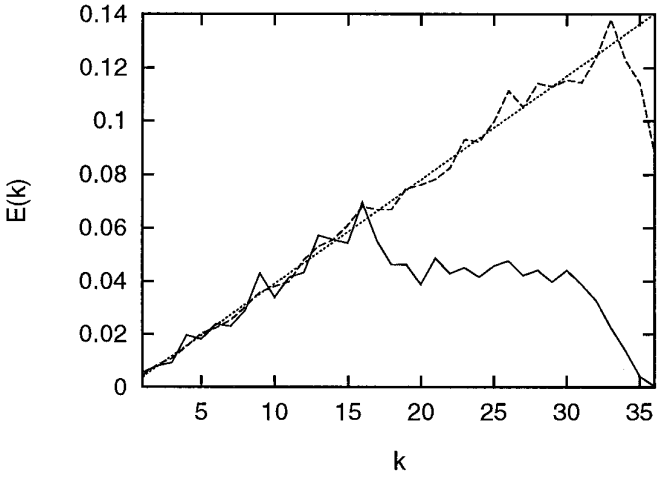

FIG. 5. Radial energy spectrum $E(k)$ without (—) and with (---) compensation for shell limitations for the corner modes from 2D inviscid simulation versus $k = (k_x^2 + k_y^2)^{1/2}$, $E(k) \approx k$ $(\cdots)$.

nomena which occur in simulations where standard numerical methods are applied.

Time-averaged radial component spectra as well as one-dimensional spectra from the simulations compare well with the predicted spectra. In Figure 5 we show two different energy spectra. The area under the full curve corresponds to the actual kinetic energy contained in the computational domain. As a consequence of integrating over partial shells for $k > N_y = 16$ (the corner modes) the energy drops sharply toward higher wavenumbers. If we apply the usual correction, i.e., we compensate for incompleteness in the integration surface by multiplying with $\pi k/S(k)$ (or $4\pi k^2/S(k)$ in 3D), where $S(k)$ is the number of samples in the kth shell, we obtain the dotted curve which follows the expected k^1 law of inviscid, isotropic, random phase 2D turbulence. The ability to recover the correct spectral shape from the simulation together with the good agreement with analytical predictions shows that the "artificial" anisotropy is purely kinematic. If grid anisotropy would change dynamics by introducing an unphysical force it should show up in such a test. It would be interesting to see how other numerical schemes in use for simulation of turbulence perform in such a test.

3.3. *Weight Factor Correction for Isotropic Turbulence*

As mentioned in the preceding section, in the special case of isotropic turbulence the shape of the scalar energy spectrum function $E(k)$ can be corrected with a weight factor which is applied to the corner mode shells. This weight factor can be deduced from purely geometrical considerations since energy is distributed equally in a given shell centered around the origin of wavespace.

Similarly, weight factors for individual components of Φ_{ij} can be constructed based on the assumption of *isotropy* of the flow field under consideration. This assumption will not be met by most real flows. Therefore, these weights will be of limited use for practitioners. A general applicable correction for spectra of energy or individual velocity components in arbitrary flows requires knowledge of the spectrum tensor near the cutoff in wavespace. Usually, this information is not available. However, it might be possible to construct approximative weights by an extrapolation procedure using information about the resolved scales of motion near the cutoff and making assumptions about changes in the spectrum tensor with increasing wavenumber.

In the following we briefly outline the procedure to compute weights $W_1(k)$, $W_2(k)$ in case of two-dimensional, isotropic turbulence for compensation of the corner mode shells $\min(N_x, N_y) < k < (N_x^2 + N_y^2)^{1/2}$ of the radial spectra $E_{11}(k)$ and $E_{22}(k)$. As in the computation of radial spectra (Eqs. (11) and (12)) we integrate the projection operator $\delta_{ij} - k_i k_j/k^2$ over the part of the shell k which lies inside the region bordered by N_x, N_y, N_z. The weights are then computed as the ratio of the integral evaluated over a complete shell and the integration over a partial shell. With

$$\int_0^{2\pi} \left(1 - \frac{k_x^2}{k^2}\right) k \, d\theta = \int_0^{2\pi} \left(1 - \frac{k_y^2}{k^2}\right) k \, d\theta = k\pi \qquad (15)$$

we obtain

$$W_1(k) = \frac{\pi}{4\int_{\theta_a}^{\theta_b} \sin^2\theta \, d\theta}, \quad W_2(k) = \frac{\pi}{4\int_{\theta_a}^{\theta_b} \cos^2\theta \, d\theta}. \qquad (16)$$

The integration bounds are given in Eq. (13). The weights are plotted in Fig. 1 for the case $N_x/N_y = 2$. They are valid for isotropic 2D turbulence with arbitrary scalar spectrum function $E(k)$. Using these factors to compensate spectra $E_{11}(k)$ and $E_{22}(k)$ recovers the relation $E_{11}(k) = E_{22}(k) \approx k$ over the entire wavenumber range under consideration; see Fig. 1.

In a similar manner weight factors can be constructed for isotropic 3D turbulence. In this case the integrals must be evaluated numerically and the definition of integration bounds is more involved; see [11]. Again, we emphasize that these weights will be of limited use since the assumption of (local) isotropy will not be met in most situations where it might be desirable to apply a correction to radial spectra in order to deduce a meaningful measure of anisotropy of scales of motion in a certain wavenumber range.

3.4. *Three-Dimensional Euler Flow*

From Fig. 5 it is evident that Euler flow will be affected strongly by grid anisotropy because most of the energy

TABLE I

Unphysical Anisotropy of 3D Euler Flow Caused by an Anisotropic Mesh

		$\overline{u}'/\overline{v}'$		$\overline{u}'/\overline{w}'$	
N_x/N_y	N_x/N_z	Eq. (4)	Simulation	Eq. (4)	Simulation
2	2	0.76	0.74	0.76	0.74
2	4	0.71	0.68	0.64	0.63

resides on outer shells, i.e., near the cutoff wavenumber. Since spectra decay toward the wavenumber cutoff in viscous flows the grid anisotropy will be a minor problem as long as the flow is well resolved as in DNS. However, as demonstrated later, the grid anisotropy will have a noticeable impact in those LES which are only marginally resolved.

Extension of the analysis to 3D Euler flow is straightforward and we report a few results only. The integration (Eq. (4)) must be carried out numerically. In [11] an expression similar to Eq. (4) was integrated over a rectangular subdomain of wavespace using spherical coordinates. We use Cartesian coordinates and discretize the **k**-space subdomain in equal-sided cubes. The discretization has been refined until the result did not change by more than 1% for two subsequent refinement steps.

Table I compares predicted velocity component ratios with those obtained from actual 3D inviscid simulations. The small deviations are probably a result of using only a small number of modes ($N_x = 16$, $N_y = 8$, $N_z = 4$) in the simulations. For a given cell aspect ratio a_{xy} the deviation of velocity ratios from 1 is smaller in the 3D case (25%) than in the 2D (33%) case. This can be explained in terms of the additional third dimension: in 3D a shell with radius k of spectra E_{11} and E_{22} will have contributions from modes k_z which do not depend much on a_{xy}. As a consequence, contributions from modes k_x and k_y which are sensitive with respect to a_{xy} do not count as much as in the corresponding 2D case.

4. MODEL SPECTRA FOR VISCOUS FLOW

4.1. *Isotropic Turbulence on Anisotropic Grids*

In order to estimate the role of grid anisotropy for a situation with a more realistic energy distribution that might be encountered in an actual LES we use a model spectrum for isotropic turbulence of the form

$$\begin{aligned} E(k) &= Ak^4 \qquad \text{for } 0 < k < k_{\text{peak}}, A = k_{\text{peak}}^{-5} \\ E(k) &= k^{-1} \qquad \text{for } k_{\text{peak}} < k < k_{\text{d}}, \\ E(k) &= Bk^{-2} \qquad \text{for } k > k_{\text{d}}, B = k_{\text{d}}. \end{aligned} \tag{17}$$

In the following examples we use $k_{\text{peak}} = 4$, $k_{\text{d}} = 24$ and vary the cutoff wavenumbers N_x, N_y, N_z. The model spectrum is shown in Fig. 7. The choice of a k^{-1} range in the spectrum is partially motivated by the findings of Piomelli [7], who reports even shallower slopes for near wall spectra obtained in a LES of turbulent channel flow. The smallest value for the cutoff is $k_{\text{c}} = 12$, leaving a minimum of one octave of wavenumbers between energy peak and nearest cutoff. This seems to be a realistic scenario for a marginally resolved LES. For this model spectrum we compute the ratio of SGS kinetic energy e and total kinetic energy $e + E$ as a function of cutoff wavenumber k_{c} as

$$\frac{e}{e+E} = \frac{\ln(k_{\text{d}}/k_{\text{c}}) + 1}{\ln(k_{\text{d}}/k_{\text{peak}}) + 6/5}. \tag{18}$$

In the following examples we use an equivalent cutoff wavenumber $k_{\text{eq}} = 24$, corresponding to a 33% contribution from SGS motions.

We obtain predictions for the resolved rms velocity fluctuations by solving Eq. (4) numerically on a rectangular domain using Eq. (2) as integrand with $E(k)$ replaced by the model spectrum from Eq. (17).

Columns 4 and 5 of Table II list rms velocity ratios resulting from discrete approximation of the model spectrum for various cutoff wavenumber ratios. For a grid aspect ratio $a_{xy} = 4:1$ the ratio $\overline{u}'/\overline{v}'$ deviates by 7% from the correct isotropic value of 1.0. As expected, the unphysical anisotropy is much smaller than that in the inviscid case. However, the viscous example shows that the effect should not be ignored in a situation which might be encountered in high Reynolds number LES where a substantial part of the kinetic energy resides in subgrid scales. From Fig. 6 it becomes evident that the effect becomes negligible if the subgrid scales contribute less than 10% to the total kinetic energy (for the chosen model spectrum shape). As seen previously in the inviscid case the effect of grid anisotropy is restricted to the high-wavenumber end of the spectrum; see Fig. 7. Again, the spectrum of the u-component is affected most strongly whereas the v-component exhibits the smallest deviation from the correct power law.

4.2. *Anisotropic Turbulence on Anisotropic Grids*

Of particular interest for high Reynolds number LES is the treatment of the near wall zone in which turbulence is highly anisotropic. As for isotropic turbulence we expect that anisotropy measures for anisotropic turbulence will depend on grid aspect ratios of the discrete representation. Quantitative results can be gained using analytical solutions for model spectrum tensors derived with rapid distortion theory (RDT) by [1, 12]. RDT of homogeneous shear flow gives a close description of many features of near wall turbulence [4].

TABLE II

Ratios of Velocity Fluctuations Obtained from Model Spectra and RDT for Various Cutoff Wavenumber Combinations

			Isotropic		Strain: $c = 2$			Shear: $\beta = 2$		
N_x	N_y	N_z	$\overline{u}'/\overline{v}'$	$\overline{u}'/\overline{w}'$	$\overline{u}'/\overline{v}'$	$\overline{u}'/\overline{w}'$	$\overline{v}'/\overline{w}'$	$\overline{u}'/\overline{v}'$	$\overline{u}'/\overline{w}'$	$\overline{v}'/\overline{w}'$
24	24	24	1.	1.	0.572	0.572	1.	1.687	1.109	0.704
48	12	24	0.936	0.982	0.554	0.601	1.085	1.757	1.099	0.625
12	48	24	1.068	1.049	0.568	0.555	0.973	1.704	1.200	0.657

Note. Listed are three cases: isotropic turbulence represented on anisotropic meshes, initially isotropic turbulence subject to axisymmetric compression, and initially isotropic turbulence subject to mean shear.

We have evaluated Eq. (4) with model spectrum tensors for two cases. The first anisotropic model case is an axisymmetric contraction with the components of the strain tensor given as $e_1 = c$ and $e_2 = e_3 = 1/\sqrt{c}$. The components of the energy spectrum tensor as a function of the initially isotropic spectrum $E(k)$ and strain c were derived by [1] and are given in the Appendix. Analytical integration in spherical coordinates yields for $c = 2$ velocity ratios $u/v = u/w = 0.571$ for turbulence not being affected by grid anisotropy. This value is independent of the form of the initial spectrum as long as the initial turbulence is isotropic.

Columns 6 to 8 of Table II list the resulting velocity ratios if the RDT solution is represented on a cubical domain with different cutoff wavenumber combinations. For isotropic cutoff with $N_x = N_y = N_z = 24$ the analytical result from [1] is recovered. Anisotropic representation causes unphysical deviations from the correct velocity ratios. The largest deviation is found for the ratio $\overline{v}'/\overline{w}'$ and amounts to nearly 9% for the given model spectrum. This example demonstrates that the strongest side effect of grid anisotropy on Reynolds stress anisotropy is not necessarily found for the velocity ratio which corresponds to the maximum grid anisotropy, i.e., $a_{xy} = 0.25$ in this case. As explained in Section 3 the anisotropy defect for individual spectrum tensor components depends on the wavevector orientation. The distribution of Φ_{ij} in a particular shell k is characteristic for the turbulence field being analyzed and varies considerably among the components (see equations in the Appendix). It is evident that anisotropic filtering affects each component in its specific way which prevents the construction of universal weight functions to compensate for this effect.

Radial spectra from turbulence subject to axisymmetric compression are plotted in Fig. 8 for two different grid anisotropy values. The radial spectral E_{22} and E_{33} are identical for $k < 12$. The scale-dependent anisotropy varies

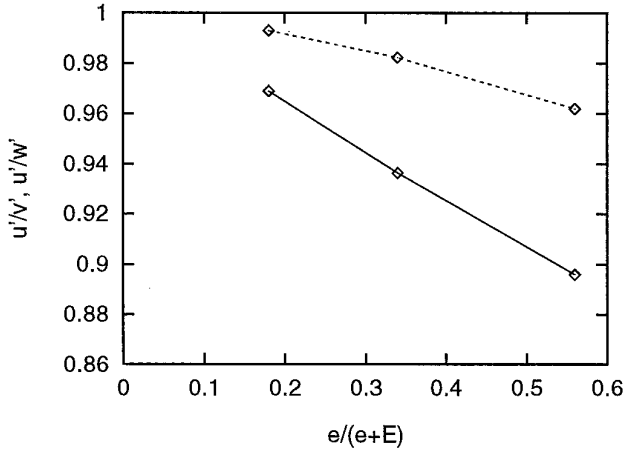

FIG. 6. Rms ratio $\overline{u}'/\overline{v}'$ (—) and $\overline{u}'/\overline{w}'$ (---) versus ratio of subgrid scale kinetic energy and total kinetic energy obtained by applying an anisotropic filter with cutoff wavenumber ratios $N_x:N_y:N_z = 4:1:2$ to isotropic turbulence following the model spectrum given in Eq. (17).

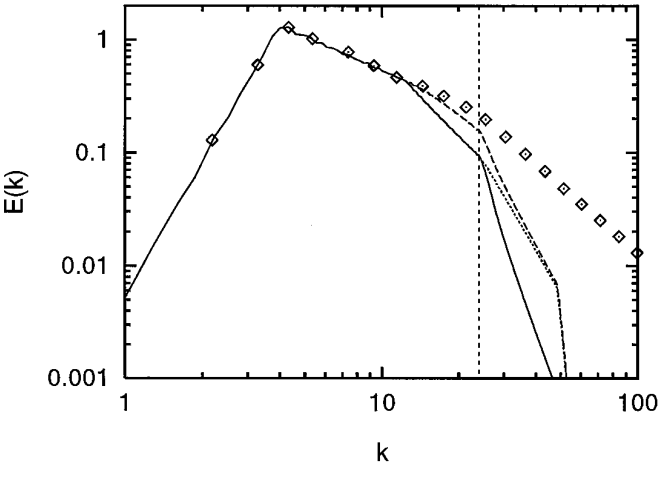

FIG. 7. Radial spectra for nominally isotropic turbulence following Eq. (17) represented on an anisotropic mesh with $N_x = 48$, $N_y = 12$, $N_z = 24$. Lines represent $E_{11}(k)$ (—), $E_{22}(k)$ (---), and $E_{33}(k)$ ($\cdots$). The symbol $\diamond$ marks the spectrum of the unfiltered model field. The vertical line marks the equivalent cutoff wavenumber $k_{eq} = 24$.

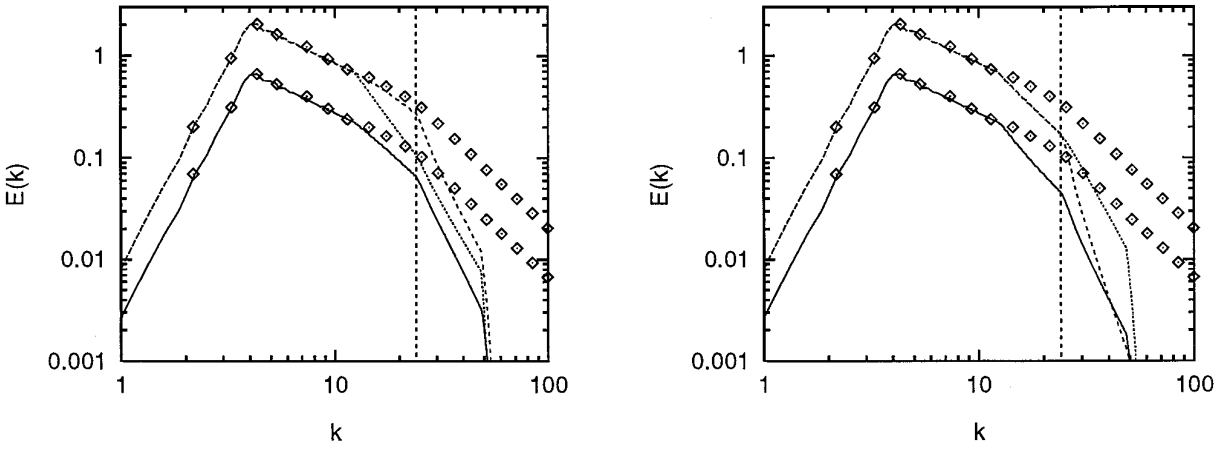

FIG. 8. Radial spectra for initially isotropic turbulence subject to axisymmetric compression. Left: Cutoff wavenumbers at $N_x = 48$, $N_y = 12$, $N_z = 24$; right: cutoff at $N_x = 12$, $N_y = 48$, $N_z = 24$. Lines represent $E_{11}(k)$ (—), $E_{22}(k)$ (---), and $E_{33}(k)$ ($\cdots$). The symbol $\diamond$ marks spectra of the unfiltered model field. The vertical line marks the equivalent cutoff wavenumber $k_{eq} = 24$.

considerably in the wavenumber range in between minimum and maximum cutoff numbers, depending on the ratios of N_x, N_y, and N_z. For example, in the configuration with $N_x = 48$, $N_y = 12$, $N_z = 24$ the spectra E_{11} and E_{22} are not affected nearly as much as E_{33} in the range $12 < k < 24$.

Our second anisotropic example is homogeneous shear flow. The change of the energy spectrum tensor as a function of applied total shear is given by [12] and in corrected form by [8] (see Appendix). We have investigated grid anisotropy effects for a moderate amount of total shear $\beta = dU/dy * t = 2$ applied to initially isotropic turbulence. Results are tabulated in the last two columns of Table II. Qualitatively similar results are obtained for $\beta = 4$. In our isotropic examples we found a qualitative correspondence between grid anisotropy and Reynolds stress tensor anisotropy. Here we find—as for turbulence subject to axisymmetric compression—that it is no longer possible to predict changes in velocity ratios from corresponding changes in grid anisotropy. For example, velocity ratios which involve the spanwise velocity component $\overline{w}'$ are more affected by grid anisotropy than the ratio $\overline{u}'/\overline{v}'$ although the corresponding grid anisotropy a_{xy} is the largest. This is consistent with the shape of the variance spectra depicted in Fig. 9. Spectra E_{11} and E_{22} are less affected by grid anisotropy than E_{33}.

As mentioned earlier it is impossible to derive a general correction (weight factors) since for an arbitrary flow the distribution of Φ_{ij} in a given shell k is not known. The example of shear flow demonstrates nicely that in certain circumstances an anisotropic representation can be the most economic for a given flow if the grid anisotropy mirrors to a certain degree the spatial properties of the particular spectrum tensor. In the case of shear flow dominant structures (low-wavenumber modes) will be aligned with the mean shear direction which explains why representation on an anisotropic grid with $\Delta x > \Delta y$ gives acceptable values for the ratio $\overline{u}'/\overline{v}'$ in this case.

5. ANISOTROPIC GRID FILTER IN THE INERTIAL SUBRANGE

If the anisotropic cutoff, characterized by the equivalent wavenumber $k_{eq} = 2\pi/\Delta_{eq}$, is in the inertial subrange the SGS kinetic energy can be estimated from $e = (\nu_t/(c_\nu \Delta_{eq}))^2$, where $c_\nu = 0.0856$ and ν_t denotes the SGS eddy viscosity [9]. Assuming local isotropy and a $k^{-5/3}$ power law extending to

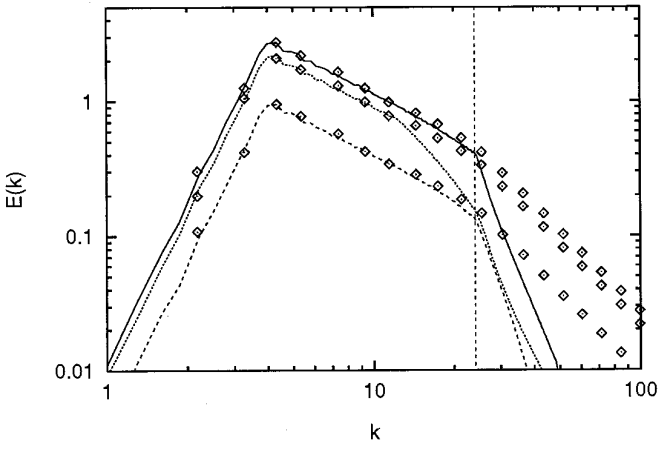

FIG. 9. Radial spectra for turbulence subject to mean shear with cutoff wavenumbers at $N_x = 12$, $N_y = 48$, $N_z = 24$. Lines represent $E_{11}(k)$ (—), $E_{22}(k)$ (---), and $E_{33}(k)$ ($\cdots$). The symbol $\diamond$ marks spectra of the unfiltered model field. The vertical line marks the equivalent cutoff wavenumber $k_{eq} = 24$.,

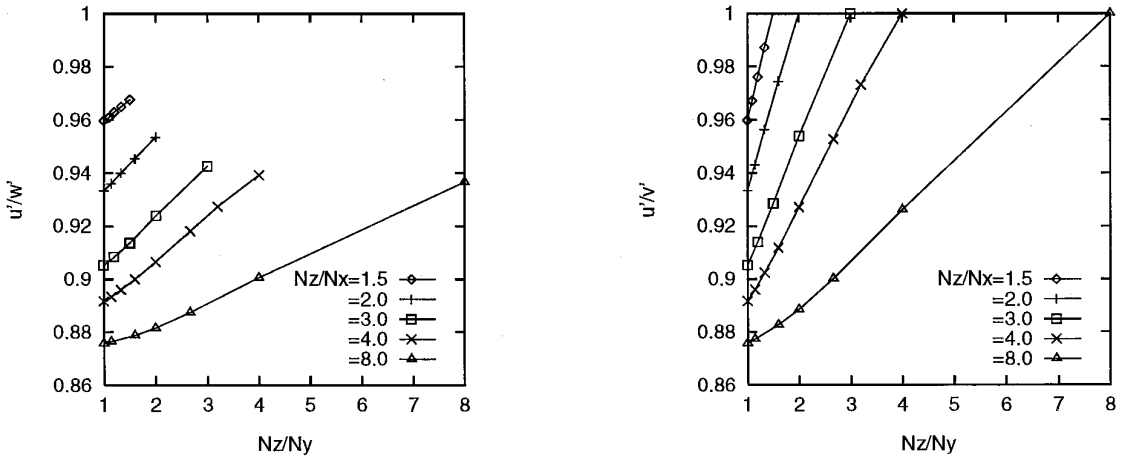

FIG. 10. Anisotropy of SGS normal stresses measured as $(\tau_{11}/\tau_{33})^{1/2}$ (left) and $(\tau_{11}/\tau_{22})^{1/2}$ (right) for turbulence with anisotropic cutoff in the inertial subrange as a function of cutoff wavenumber ratios.

infinity we obtain SGS normal stresses by integrating Eq. (2) over the entire wavespace with the rectangular subdomain $|k_x| < N_x$, $|k_y| < N_y$, $|k_z| < N_z$ excluded. For this integration we split the region in two parts: the integration is done numerically for an inner region bounded by N_x, N_y, N_z and the first complete shell, i.e., $k_{\text{lim}} = (N_x^2 + N_y^2 + N_z^2)^{1/2}$. For the remaining (outer) region we use

$$\tau_{11,\text{out}} = \tau_{22,\text{out}} = \tau_{33,\text{out}} = c \int_{k_{\text{lim}}}^{\infty} k^{-5/3}\, dk = \frac{3}{2} c k_{\text{lim}}^{-2/3}, \quad (19)$$

with c determined from $E_{ii}(k_{\text{lim}})$. The "artificial" anisotropy is solely a result of integration over incomplete shells in the inner region. The anisotropy of the stress contribution from the inner subregion will be "diluted" by the isotropic outer part stresses $\tau_{ii,\text{out}}$. We have computed SGS normal stresses for various combinations of N_x, N_y, and N_z. The resulting anisotropy measures $(\tau_{11}/\tau_{33})^{1/2}$ and $(\tau_{11}/\tau_{22})^{1/2}$ are depicted in Fig. 10. We find that even for moderate aspect ratios of $a_{xy} = 4$ individual normal stresses τ_{11} and τ_{22} deviate by approximately 20%. Clearly, splitting the subgrid kinetic energy into three equal parts is unacceptable for anisotropic meshes. However, this is only relevant in these situations which require specific knowledge of SGS properties, e.g., modeling of scalar transport in the context of chemical reactions. In order to obtain an inertial subrange near the cutoff in an LES of inhomogeneous flow several decades of wavenumbers must be resolved between energy peak and cutoff. In this case SGS stresses will contribute only a few percent to the total stresses. Then, for the anisotropy of *total* stresses it will be of little relevance whether the anisotropy of SGS stresses is known exactly.

6. CONCLUSIONS

We have studied the effect of separating a turbulence field in resolved and subgrid scale motions by means of an anisotropic grid filter which we define as the cutoff in Fourier space. A numerical example employing standard finite differences demonstrates that the choice of Fourier cutoff is indeed a valid and useful description of the grid filter in the context of finite differences or finite volumes. By integrating the energy spectrum tensor for various model turbulence flows over anisotropic **k**-space subregions we have demonstrated that it is misleading to characterize the decomposed parts by common anisotropy measures.

Our results show that in situations which might be encountered in high Reynolds number LES the deviations between traditional anisotropy measures (based on resolved and SGS stress tensors) and physical meaningful alternatives (based on isotropic cutoff in wavespace at the equivalent wavenumber k_{eq}) can be significant and must be taken into account when judging the anisotropy state of resolved or SGS stresses separately. The deviation from a physical meaningful anisotropy state depends on various parameters such as the energy spectrum shape near the cutoff in wavespace, the cell aspect ratios, and the range of scales which are resolved.

The effect is purely kinematic and is primarily a problem of interpretation of simulation data. We do not say that anisotropic grids should not be used for turbulence simulation. On the contrary, anisotropic grids will guarantee the most economical representation of the flow if the grid anisotropy mirrors some properties of the specific energy spectrum tensor—a well-known fact which has been widely used in the past.

Quantitative statements apply to a specific situation only. We have shown that for a model spectrum exhibiting k^{-1} decay for intermediate scales and k^{-2} decrease toward small scales even for moderate aspect ratios $\Delta x/\Delta y = 4$ the ratios of rms values of resolved scale fields can differ by up to 10% from the correct ''physical'' values which would be obtained by strictly isotropic cutoff. The particular situation represents a rather marginally resolved flow with about one octave of wavenumbers between energy peak and minimum cutoff wavenumber and SGS motions contributing more than 30% to the total kinetic energy.

In high Reynolds number LES it seems unavoidable that certain regions of a flow will be marginally resolved. There and in cases where the near wall zone is modeled our findings apply. RANS models have been proposed where model parameters depend on stress tensor anisotropy. If SGS models of this type are devised one should be aware of the grid anisotropy issue. Finally, modeling chemical reactions or subgrid scale scalar transport in the framework of LES requires a precise knowledge of SGS stresses.

With the cutoff in the inertial subrange it is possible to account for grid anisotropy when estimating normal stresses. We have shown how weight factors can be derived for the spectrum tensor components if we assume the turbulence to be isotropic in the range of scales under consideration.

No general correction for grid anisotropy effects can be constructed without knowing the energy spectrum tensor close to the cutoff. It might be possible to develop approximative correction factors by an extrapolation procedure which is based on available information of the resolved flow. Another way of obtaining more physical sound information about the anisotropy state of resolved scale motion of an LES would consist in defining an additional (less) resolved field. This would be obtained by selectively filtering the field in certain directions with the overall goal of reducing the anisotropy of the grid filter. Anisotropy measures of the resolved scales should then be based on this filtered field.

APPENDIX

The components of the spectrum tensor for turbulence subject to axisymmetric contraction with strains $e_1 = c$, $e_2 = e_3 = 1/\sqrt{c}$ in the RDT approximation read with $\chi^2 = k_x^2/c^2 + c(k_y^2 + k_z^2)$

$$\Phi_{11}(\mathbf{k}, c) = \frac{E(k)}{4\pi\chi^4}[k_y^2 + k_z^2]$$

$$\Phi_{22}(\mathbf{k}, c) = \frac{E(k)}{4\pi\chi^4 k^2 c^3}[k_y^2(k_x^2 + c^6 k_z^2) + (k_x^2 + c^3 k_z^2)^2]$$

$$\Phi_{33}(\mathbf{k}, c) = \frac{E(k)}{4\pi\chi^4 k^2 c^3}[k_z^2(k_x^2 + c^6 k_y^2) + (k_x^2 + c^3 k_y^2)^2].$$

Individual components of the spectrum tensor of homogeneous turbulence subject to shear in the RDT approximation read

$$\Phi_{11}(\mathbf{k}, \beta) = \frac{E(k)}{4\pi k^2}\left[\frac{k^2}{k_x^2 + k_z^2} Q_1 \left(Q_1 - \frac{2k_x k_y}{k^2}\right) + \frac{k_y^2 + k_z^2}{k^2}\right]$$

$$\Phi_{22}(\mathbf{k}, \beta) = \frac{E(k)}{4\pi k^2}\frac{k^2(k_x^2 + k_z^2)}{(k^2 - 2\beta k_x k_y + \beta^2 k_x^2)^2}$$

$$\Phi_{33}(\mathbf{k}, \beta) = \frac{E(k)}{4\pi k^2}\left[\frac{k_x^2 k_z^2}{(k_x^2 + k_z^2)k^2} Q_3^2 - \frac{2k_x k_y k_z^2}{k^2(k_x^2 + k_z^2)} Q_3 + \frac{k_x^2 + k_y^2}{k^2}\right]$$

$$\Phi_{12}(\mathbf{k}, \beta) = \frac{E(k)}{4\pi k^2}\frac{k^2 Q_1 - k_x k_y}{k^2 - 2\beta k_x k_y + \beta^2 k_x^2},$$

where $k^2 = k_x^2 + k_y^2 + k_z^2$. The parameter β denotes the total amount of shear applied to the isotropic field with initial spectrum $E(k)$. Q_1 and Q_3 are defined as

$$Q_1(\mathbf{k}, \beta) = -\frac{k_z^2}{k_x(k_x^2 + k_z^2)^{1/2}} \arctan\left[\frac{\beta k_x (k_x^2 + k_z^2)^{1/2}}{k^2 - \beta k_x k_y}\right] + \frac{\beta k_x^2(k^2 - 2k_y^2 + \beta k_x k_y)}{k^2(k^2 - 2\beta k_x k_y + \beta^2 k_x^2)}$$

$$Q_3(\mathbf{k}, \beta) = +\frac{k^2}{k_x(k_x^2 + k_z^2)^{1/2}} \arctan\left[\frac{\beta k_x (k_x^2 + k_z^2)^{1/2}}{k^2 - \beta k_x k_y}\right] + \frac{\beta(k^2 - 2k_y^2 + \beta k_x k_y)}{k^2 - 2\beta k_x k_y + \beta^2 k_x^2}.$$

ACKNOWLEDGMENT

I am grateful for valuable suggestions of Dr. T. S. Lund on a draft of this paper.

REFERENCES

1. G. K. Batchelor, *The Theory of Homogeneous Turbulence* (Cambridge Univ. Press, Cambridge, UK, 1953).
2. J. W. Deardorff, A numerical study of three-dimensional turbulent channel flow at large Reynolds numbers, *J. Fluid Mech.* **41,** 453 (1970).
3. M. Germano, U. Piomelli, P. Moin, and W. H. Cabot, A dynamic subgrid-scale eddy viscosity model, *Phys. Fluids A* **3,** 1760 (1991).
4. M. J. Lee, J. Kim, and P. Moin, Structure of turbulence at high shear rate, *J. Fluid Mech.* **212,** 561 (1990).
5. C. Meneveau, Statistics of turbulence subgrid-scale stresses: Necessary conditions and experimental tests, *Phys. Fluids* **6,** No. 2, 815 (1994).

6. P. Moin and J. Kim, Numerical investigation of turbulent channel flow, *J. Fluids Mech.* **118,** 341 (1982).
7. U. Piomelli, High Reynolds number calculations using the dynamic subgrid-scale stress model, *Phys. Fluids A* **5,** 1484 (1993).
8. W. C. Reynolds, Fundamentals of turbulence for turbulence modeling and simulation, Notes for ME 261B (Department of Mechanical Engineering, Stanford University, Stanford, CA), [Unpublished]
9. H. Schmidt and U. Schumann, Coherent structure of the convective boundary layer derived from large eddy simulation, *J. Fluid. Mech.* **200,** 511 (1989).
10. U. Schumann, Subgrid scale model for finite difference simulations of turbulent flows in plane channels and annuli. *J. Comp. Phys.* **18,** 376 (1975).
11. A. Scotti, C. Meneveau, and D. K. Lilly, Generalized Smagorinsky model for anisotropic grids, *Phys. Fluids A* **5,** No. 9, 2306 (1993).
12. A. A. Townsend, *The Structure of Turbulent Shear Flow,* 2nd ed. (Cambridge Univ. Press, Cambridge, UK, 1976).